Breakdown of Feynman scaling in high-energy cosmic-ray interactions

M. Shibata
Department of Physics, Faculty of Education, Yokohama National University, Hodogaya-ku, Yokohama 240, Japan
(Received 20 April 1981)

Extensive Monte Carlo calculation on γ-ray families was carried out under appropriate model parameters which are currently used in high-energy cosmic-ray phenomenology. Characteristics of γ-ray families are systematically investigated by the comparison of calculated results with experimental data obtained at mountain altitudes. The discussion is devoted mainly to examining the validity of Feynman scaling in the fragmentation region of multiple-meson production. It is concluded that the experimental data cannot be reproduced under the assumption of the scaling law if primary cosmic rays are dominated by protons. Other possibilities on primary composition and increase of interaction cross section are also examined. These assumptions are consistent with experimental data only when we introduce intense dominance of heavy primaries in the high-energy region and very strong increase of the interaction cross section (say $\sigma \propto E_0^{\,0.06}$) simultaneously. Otherwise, the breakdown of Feynman scaling in the fragmentation region and the existence of azimuthal asymmetry in production mechanism are strongly suggested by high-energy cosmic-ray interactions ($E_0 \gtrsim 10^{15}$ eV).

I. INTRODUCTION

There has been a long history of the study of multiparticle production induced by very-high-energy cosmic rays whose incident energy covers a wide range of 10^{11}–10^{16} eV or even more, depending on the type of experiment. Emulsion-chamber experiments at mountain altitudes provide us with information on multiparticle production in the 10^{14}–10^{16} eV region through the observation of γ and hadron families which are the bundle of electromagnetic and hadronic particles produced by the interactions of a high-energy cosmic ray with atmospheric nuclei. Usually the observable quantities are related to the information of several successive interactions attributed to the same primary cosmic radiation.

Several phenomenological models were proposed to interpret production mechanism since the early 1950's. Among them, the two-fireball model[1] could attractively explain some characteristics of cosmic-ray phenomena. But during the last decade, accelerator physics in the 10^{10}–10^{12} eV region proved a remarkable feature of multiproduction called Feynman scaling[2] or the hypothesis of limiting fragmentation.[3] It became one of the most important problems in cosmic-ray physics to examine the validity of the scaling law in a higher-energy region than is available at present accelerators. The two-fireball model, or, generally speaking, the high-multiplicity model, proposes a fast increase of multiplicity as $n \propto E_0^{\alpha}$, where α is $\frac{1}{4}$–$\frac{1}{2}$ while the scaling law implies a logarithmic increase with the incident energy E_0. The production spectrum of secondaries of these two models also differs greatly.

Since the cosmic-ray experiment brings us indirect information on elementary processes as mentioned before, direct comparison of experimental data with theoretical predictions is usually impossible and Monte Carlo simulation based on given assumptions provides us with an interpretation of the experimental data. There are two independent calculations connected with the Mt. Fuji emulsion-chamber experiment[4] which are utilized as the basis of the analysis of experimental data. One of them is described in the present paper and another work by Kasahara *et al.*[5] will be published elsewhere. The consistency of the two calculations will be discussed later, together with some other works.[6]

Among a number of possibilities to be assumed in the process of the propagation of cosmic rays through the atmosphere, the following parameters are adopted as standard ones which are based on the extrapolation of the low-energy data.

Standard model.

(1) Primary particles and energy spectrum: *Proton* primary with bending slope

$$I(E)\,dE \propto E^{-\beta-1}\,dE\,, \quad \beta = \begin{cases} 1.7\,, & E < 10^{15}\text{ eV}\,, \\ 2.1\,, & E > 10^{15}\text{ eV}\,, \end{cases} \tag{1.1}$$

(2) Scaling law in particle production spectrum:

$$f(x)\,dx \propto (1-x)^{3.5}dx/x\,, \tag{1.2}$$

where $x = E/E_0$, E is the secondary energy, and E_0 denotes incident energy.

(3) Interaction cross section:

$\sigma = \text{const}$ ($\lambda_N = 80$, $\lambda_\pi = 96$ g/cm^2 in the atmosphere).

(4) Charge-exchange probability P in the process $\pi^{\pm} + \text{air} \rightarrow \pi_{\text{leading}} + X$ is $P = 0$.

(5) Mean transverse momentum:

$$\langle P_t \rangle = \begin{cases} 330\text{ MeV}/c \text{ for secondary pions}\,, \\ 500\text{ MeV}/c \text{ for leading particles}\,. \end{cases}$$

Then modifications of the model parameters can be made as follows.

Modifications of model parameters

(1′) (a) Single slope of primary energy spectrum with $\beta = 1.7$. (b) Chemical composition of primaries are included. The chemical abundances are listed in Table I, which are derived by the extrapolation of the low-energy data.[7]

(2′) Cocconi-Koester-Perkins (CKP) model[8] is used in production mechanism (violation of scaling law).

(3′) Rising cross section is assumed using the formula $\sigma \propto E^{0.06}$.

(4′) Charge-exchange probability of leading pion is assumed to be $P = \frac{1}{3}$.

(5′) Large transverse momentum is assumed using the mean value $\langle P_t \rangle = 660$ MeV/c.

Though there are many combinations of the model parameters, typical ones are tested and the characteristics of each set of parameters will be discussed later. In order to specify the assumptions used in a calculation, the following symbols are used:

P: proton primary (bending slope).
P': proton primary (single slope, $\beta = 1.7$).
M: mixed primary (bending slope).
α, CNO, Fe: purely heavy primary (bending slope).
R: rising cross section.
S: scaling model.
C: CKP model.
ch: charge-exchange probability $P = \frac{1}{3}$.

For example, a model denoted as *PRS* uses the proton primary with bending slope, rising cross section, and scaling model, while other properties such as charge-exchange probability or mean P_t are the same as the standard model. More details of the calculation are described in the next section.

A new method of analysis called "rejuvenation" was introduced by the Pamir collaboration[9] in 1975 to extract the characteristics of the production spectrum. This method uses relative threshold $f'_{\min}$ instead of the usual detection threshold (around 2 TeV), where $f'_{\min}$ is defined as

$$\frac{E_{n'}}{\sum_{i=1}^{n'} E_i} > f'_{\min}\ , \quad \frac{E_{n'+1}}{\sum_{i=1}^{n'+1} E_i} < f'_{\min}\ ,$$

when we calculate summation of energy from the highest one in decreasing order. After finding a critical value of the energy corresponding to $f'_{\min}$ for each family, the following quantities are used in the analysis:

n': rejuvenated multiplicity,
$\sum' E$: rejuvenated total γ-ray energy,
$f' = E/\sum' E$: fractional energy of constituent γ-rays.

The scaling law implies the invariance of f' spectra in different energy regions. But the opposite problem, namely, the sensitivity of rejuvenated characteristics of families to the interaction model or to other parameters, is to be examined. The present paper also deals with the analysis of rejuvenated families.

TABLE I. Mixed primary model. Chemical abundances of primaries in percent. The symbols in the first column represent groups of elements whose mean mass number is given in the second column.

A \ E_0 (eV)		10^{12}	10^{14}	10^{16}	10^{18}
p	1	37.5	18.6	6.8	2.1
α	4	18.8	9.6	3.6	1.1
L	8	0.7	0.2	0.06	0.01
M	15	15.2	19.8	18.9	15.2
LH	25	9.5	18.3	25.8	30.7
MH	35	3.7	5.8	6.7	6.5
VH	56	14.6	27.6	38.1	44.4

II. DETAILS OF SIMULATION

A. Primary particles

The calculations were made for various primary particles [i.e., protons, α particles, (C, N, O) nuclei, and irons] and with mixed chemical composition in which the dominance of heavy nuclei is assumed in the high-energy region. Figure 1 represents the primary energy spectrum of the mixed-composition model.

The proton equivalent spectrum is defined as $I_{p\text{eq}}(>E_0) = \sum_A A I_A(>AE_0)$, where A denotes mass number of the nuclei.

The slope of the proton equivalent spectrum gradually becomes steeper; $\beta \sim 1.8$ for $E_0 < 10^{13}$ eV, $\beta \sim 1.9$ for $10^{13} < E_0 < 10^{15}$ eV, and $\beta \sim 2.3$ for $E_0 > 10^{15}$ eV.

The cutoff energy of primaries coming to the top of the atmosphere is 200 TeV in the standard model and other higher values are used in modified models, for example, 300 TeV for *PRC*, 500 TeV for α, and 3000 TeV for Fe because primaries below these energies hardly create families at the observation level.

B. Interaction mean free path

Interaction mean free paths of nucleons and pions in the atmosphere are assumed to be 80 g/cm^2 and 96 g/cm^2, respectively. In case of the rising-cross-section model, these values are

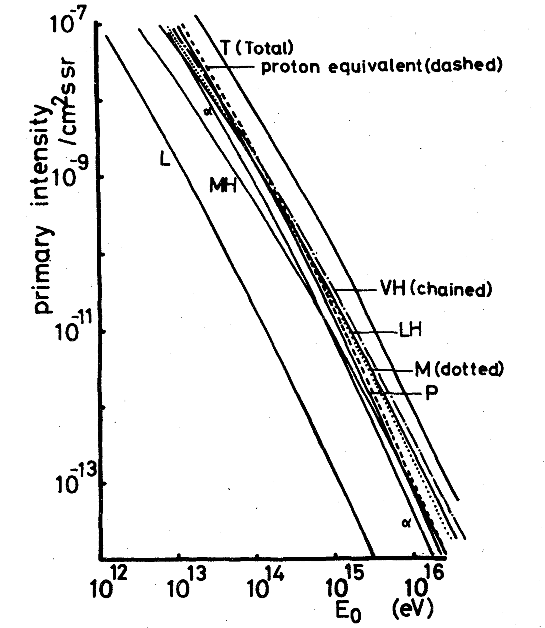

FIG. 1. Primary energy spectrum assumed in mixed composition model. Details are given in Table I. Dashed line represents proton equivalent total spectrum.

used at 1 TeV and the relation $\lambda \propto E_0^{-0.06}$ is assumed. Though this energy dependence may be too strong as an extrapolation of the accelerator data, the extreme case is tested in this paper.

C. Inelasticity

The distribution of the inelasticity coefficient is assumed to be uniform between zero and unity, both for nucleons and charged pions in the whole energy region.

D. Production spectrum and multiplicity

Two typical production spectra are tested, namely, the scaling model and the CKP model. The distribution function of variable x $(=E/E_0)$ is assumed as Eq. (1.2) for the scaling model, and as

$$f(x)dx \propto \exp(-\alpha x)dx\,, \quad \alpha = E_0^{0.25}/0.08\,, \quad E_0 \text{ in TeV} \tag{2.1}$$

for the CKP model. The technical problem of energy conservation was taken into account in the sampling method in order not to distort the assumed distribution function (see Appendix). The sampled distributions of x for scaling and CKP models are shown in Figs. 2(a) and 2(b), respectively.

The multiplicity of produced particles above 2 TeV was determined as a result of energy conservation. Mean values of sampled multiplicity of secondaries of the energy greater than 2 TeV are shown in Fig. 3 as a function of E_0.

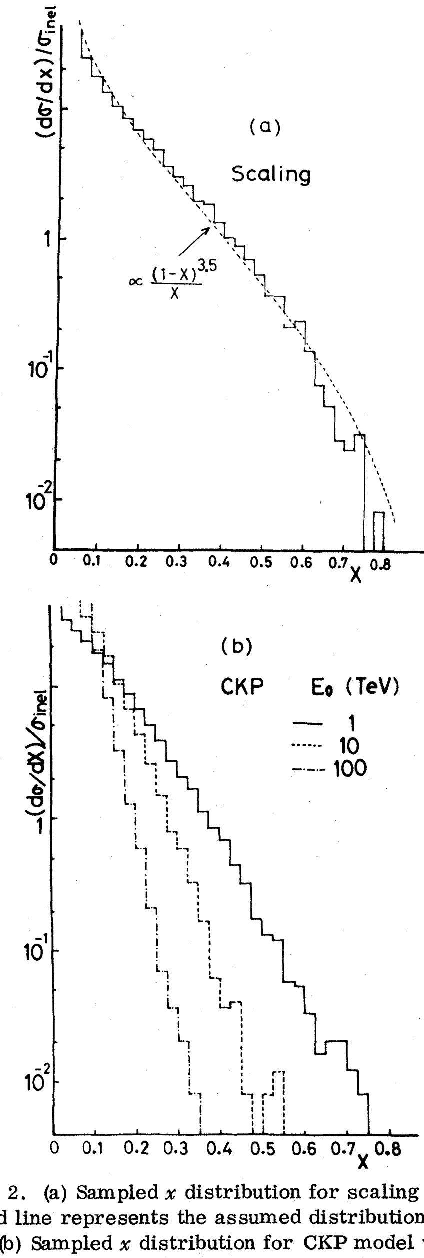

FIG. 2. (a) Sampled x distribution for scaling model. Dashed line represents the assumed distribution function. (b) Sampled x distribution for CKP model with different parent energies.

In the present calculation, scaling is defined as an invariance of normalized inclusive cross section, namely,

$$\frac{1}{\sigma}\int E\frac{d^3\sigma}{dp^3}dP_t^{\,2} = xf(x)\,.$$

Therefore no changes are assumed in the production spectrum of individual collisions even

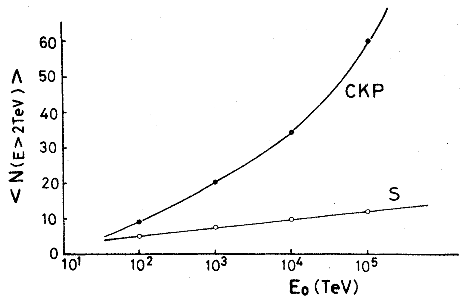

FIG. 3. Sampled average multiplicity of secondaries of the energy greater than 2 TeV. Open circle: scaling model ($n \propto \log_{10} E_0$), closed circle: CKP model ($n \propto E_0^{1/4}$).

when we include rising cross section. This seems to contradict current understanding of the scaling law which states the invariance of $E(d^3\sigma/dp^3)$, but it is still obscure to what the increase of cross section should be attributed, and the above-mentioned scheme gives an upper boundary of the effect of the fragmentation region to the observed high-energy phenomena.

The lower boundary may be obtained assuming $E(d^3\sigma/dp^3)$ invariance only for the fragmentation region and the additionally presumed pionization part (in the $x \sim 0$ region) which can reproduce the increase of cross section.

E. Transverse momentum

Sampling of transverse momentum of a secondary particle was carried out in a similar way to the fireball production model.

Firstly, the momentum of a secondary particle in a rest system is sampled using a distribution function of the form

$$f(p^*)dp^* = \frac{3}{4p_0^3} p^{*2} \exp(-p^*/p_0) dp^* ,$$

where $p_0 = 140$ MeV/c for pions and $p_0 = 213$ MeV/c for survival particles of projectiles. Secondly, zenith angle θ^* is sampled assuming isotropic distribution in a rest frame of the production system. Finally, transverse momentum is calculated as $P_t = p^* \sin\theta^*$. Thus, the distribution function of P_t is expressed as

$$f(P_t)dP_t = \frac{P_t dP_t}{4p_0^3} \int_{P_t}^{\infty} \frac{\exp(-p^*/p_0)}{[1-(P_t/p^*)^2]^{1/2}} dp^* .$$

The mean values of P_t are given as $\langle P_t \rangle = 3\pi p_0/4 = 330$ MeV/c and 500 MeV/c for pions and survival particles, respectively.

The correlation between x and P_t is not considered.

F. Model of atmosphere

The following precise formula[10] of standard atmosphere is used.

$$h(x) = 47.05 - 6.9 \ln x = 0.299[\ln(x/10)]^2 , \quad x < 25 \text{ g/cm}^2 ,$$
$$= 45.5 - 6.34 \ln x , \quad 25 < x < 230 \text{ g/cm}^2 ,$$
$$= 44.342 - 11.861 x^{0.19} , \quad 230 < x \text{ g/cm}^2 ,$$

where h denotes the height from sea level (Km) and x the atmospheric depth (g/cm^2).

G. Nucleus-nucleus interaction model

The interaction cross sections of nuclei are derived from the overlap-model formula,[11]

$$\sigma_{AB} = \pi r_0^2 (A^{1/3} + B^{1/3} - r)^2 ,$$
$$r_0 = 1.41 \times 10^{-13} \text{ cm} , \quad r = 1.17 ,$$

where A and B are the mass number of incident and target nuclei, respectively. In the nucleus-nucleus interaction, some of the nucleons interact independently and the residual part of the nucleus breaks up according to a given fragmentation parameter into lighter nuclei or nucleons. The average number of interacting nucleons is calculated by the formula[12]

$$\nu_{\text{int}} = A\sigma_{N-\text{air}} / \sigma_{A-\text{air}} ,$$

where A denotes the mass number of incident nucleus and $\sigma_{N-\text{air}}$ is the cross section of nucleon–air-nucleus interaction.

The sampling of interacting nucleons is made by binomial distribution with the above-mentioned average value. The numerical values of $\sigma_{A-\text{air}}$ and ν_{int} are listed in Table II.

The fragmentation parameter is taken from Ref. 13. The transverse momenta of fragment particles are sampled from the distribution

$$f(P_t)dP_t^2 \propto \exp(-P_t^2/2\sigma^2) dP_t^2 , \quad \sigma = 50 \text{ MeV}/c .$$

The energies of fragments are simply calculated

TABLE II. Numerical constants of nucleus-nucleus interactions. Interaction cross section $\sigma_{\text{A-air}}$ and number of interacting nucleons ν_{int} in the reaction of nucleus of mass number A in the atmosphere.

A	$\sigma_{\text{A-air}}$ (mb)	ν_{int}
1	300	1
4	505	2.38
8	662	3.63
15	865	5.20
25	1090	6.88
35	1278	8.22
56	1611	10.43

as

$$E_{\text{frag}} = E_0 A_{\text{frag}} / A .$$

H. Electromagnetic cascades

In the process of bremsstrahlung and pair creation, complete screening formulas[14] for infinite primary energy are used. Angular and lateral displacement of electrons are calculated according to multiple-Coulomb-scattering formulas.[15]

I. Secondary component

The secondary particles are assumed to be pions only and their charges are assigned by equal weight, i.e., $n_{\pi^+}:n_{\pi^-}:n_{\pi^0} = 1:1:1$. Charge conservation is not taken into account.

J. Consideration of experimental conditions

Since the threshold energy of the Mt. Fuji emulsion chamber is around 2 TeV, the minimum energy of the calculation is taken as 2 TeV for every component. The observation levels are assumed at 250, 540, 650, and 730 g/cm^2.

Hadrons coming to the observation levels interact with the lead layer of the emulsion chamber and produce jet showers (Pb jets) with mean $K_\gamma = \frac{1}{6}$. The interaction mean free path in lead is 30 cascade units (c.u.) for nucleons and 36 c.u. for charged pions. The first interaction which liberates secondary energy $\sum E_\gamma$ greater than 2 TeV is recorded with the depth of interaction in the chamber. The selection of the γ rays and hadrons is made in a way similar to the Mt. Fuji experiment; i.e., those showers of starting point less than 6 c.u. (Pb) are regarded as γ rays while others are regarded as hadrons. Therefore the contamination of hadrons into γ rays is taken into account in the calculation. The effective thickness of the chamber is assumed to be 20 c.u. for hadron detection in order to compare the results directly with experiment.

The geometrical conditions connected with the limited size of the x-ray film used in experiments (mostly 40×50 cm^2) are also considered. The centers of families are artificially positioned at random within an area of the square of 40×50 cm^2 and the particles outside of this square are rejected from analysis.

After the above-mentioned two considerations, the selection criteria of families are applied to calculate results as follows:

$$E_{\min} = 2\ \text{TeV}, \quad n_\gamma \geqslant 4, \quad \sum E_\gamma > 30\ \text{TeV}$$

$$f'_{\min} = 0.04 \text{ for rejuvenation.}$$

The number of simulated events is listed in Table III.

III. RESULTS

A. $\sum E_\gamma$ spectrum at Mt. Fuji level

The intensities of the energy flow of the γ-ray families at the Mt. Fuji level (650 g/cm^2 atmospheric depth) are calculated for various models and they are shown in Figs. 4(a)–4(d), where the perpendicular axes are normalized by the number of primaries of the energy greater than 100 TeV. The experimental data of the Mt. Fuji emulsion-

TABLE III. Integral number of simulated events.

Model \ $\sum E_\gamma$	>39 TeV	>100 TeV	>500 TeV	>1000 TeV
PS	1180	260	22	7
PRS	981	213	9	
PC	603	126	9	4
PRC	368	56	3	1
P′S	1022	270	39	
P′C	275	73	4	
P′S + ch	822	294	35	
P′C + ch	298	80	16	
PRC + ch	539	112	3	1
large P_t	143	32	2	
MS	963	252	17	5
MRS	617	137	11	1
MC	507	100	2	1
MRC	113	15		
α	398	100	11	5
CNO	327	100	15	6
Fe	242	67	8	
exp	289	118	11	5

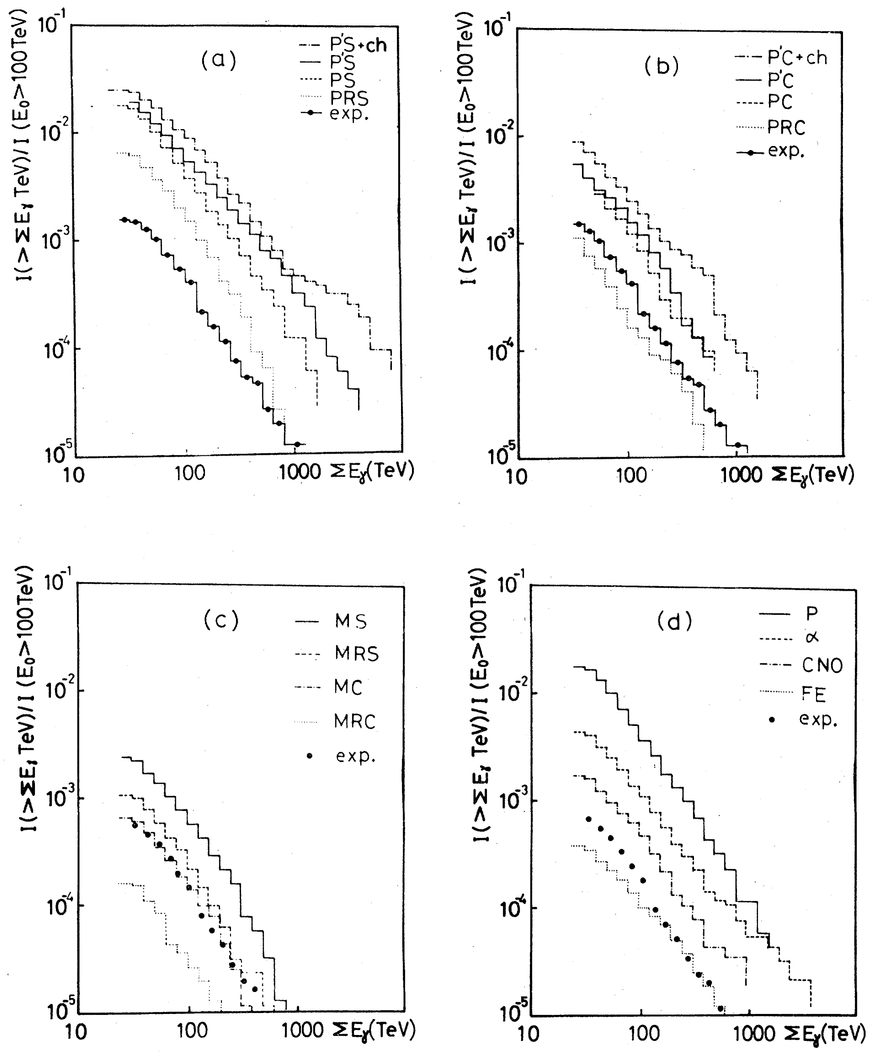

FIG. 4. (a) $\sum E\gamma$ spectrum at Mt. Fuji level (650 g/cm^2). Each model assumes proton primary and scaling law. Experimental data are normalized to proton equivalent total spectrum. (b) $\sum E\gamma$ spectrum at Mt. Fuji level. Each model assumes proton primary and CKP production spectrum. The normalization of the experimental data is the same as Fig. 4(a). (c) $\sum E\gamma$ spectrum at Mt. Fuji level. Each model assumes mixed composition. Experimental data are normalized to total primary spectrum. (d) $\sum E\gamma$ spectrum at Mt. Fuji level. Primaries are assumed as pure chemical composition; other parameters are standard.

chamber experiment are also plotted in Fig. 4, where the intensity of the primaries is assumed to be $I(E_0 > 100\ \text{TeV}) = 2.5\times10^{-9}/\text{cm}^2\ \text{sec sr}$ for the comparison with proton primary models [Figs. 4(a) and 4(b)], while $I(E_0 > 100\ \text{TeV}) = 8\times10^{-9}/\text{cm}^2$ sec sr (total energy spectrum) for the comparison with mixed-primary or purely heavy-primary models [Figs. 4(c) and 4(d)].

In Fig. 4(a), primaries are protons only and the scaling law is adopted in each model. The intensity of the standard model (PS) around $\sum E_\gamma \sim 100$ TeV is about 15 times higher than experimental data. The effect of the change in the slope of the primary energy spectrum can be seen in the difference of the intensities between PS and $P'S$ (factor $\simeq 1.3$); also the effect of the charge-exchange process of interacting charged pions can be seen in the difference between $P'S$ and $P'S$ + ch (factor $\simeq 1.7$), and in the rising cross section between PS and PRS (factor $\simeq 2.5$). Every model in Fig. 4(a) gives too high a yield of the γ-ray family; even the strong increase of the interaction cross section is not enough to obtain reasonable intensities.

The other possibilities which can decrease the intensity are the breakdown of the scaling law and/or the dominance of heavy primaries in the high-energy region. In Fig. 4(b), the comparisons are made among several models which assume proton primary and CKP production mechanisms. In this figure, the *PRC* model is consistent with experimental data within a factor of 2.

The next possibility, the dominance of heavy primary, is tested and the results are shown in Figs. 4(c) and 4(d); the former assumes mixed chemical composition in primary particles as listed in Table I (also shown in Fig. 1) and the latter assumes pure chemical composition in order to realize the effect of the mass number of primaries. In the present mixed primary model, the ratio of proton among primaries decreases rapidly in the high-energy region and *M*, *LH*, and *VH* nuclei become dominant; therefore the yield of the γ-ray family becomes less than the case of purely proton primarily due to the fast dissipation of the energy by the fragmentation process of the nucleus in the atmosphere.

In Fig. 4(d), it is seen that we need to assume purely iron primary to obtain the intensity of a γ-ray family close to the experimental value if we do not include any other possibilities such as rising cross section or break down of the scaling law.

However, it will be shown later that such a drastic assumption fails in the lateral structure of the family. In Fig. 4(c), it is shown that models *MC* and *MRS* are consistent with experimental data within a factor of 3. The relative values of the intensity of the calculated γ-ray families to the experimental data around $\sum E_\gamma \simeq 100$ TeV are summarized in Table IV.

B. Altitude variation of γ-ray families

The observation levels are assumed at various atmospheric depths in the simulation, namely, at 250, 540, 650, and 730 g/cm^2 to obtain the altitude variation of the intensity of the γ-ray families. The results are shown in Figs. 5(a) and 5(b) for proton-primary and mixed-primary models, respectively.

The attenuation lengths for each model are listed in Table V. The *PS* model gives too large a value compared with experimental data.

Not only the assumption of the rising cross section but also the CKP model and/or dominance of the heavy primary can shorten the attenuation

TABLE IV. The relative intensity of the γ-ray families around $\sum E_\gamma \simeq 100$ TeV to the experimental data of Mt. Fuji.

Model	I(calc)/I(exp)	Model	I(calc)/I(exp)
PS	14.3 ±1.7	*MS*	6.7 ±1.0
P′S	19 ±3	*MRS*	2.5 ±0.4
P′S + ch	33 ±4	*MC*	1.7 ±0.3
PRS	5.8 ±0.8	*MRC*	0.30 ±0.11
PC	3.5 ±0.5	α	14.0 ±2.0
P′C	5.8 ±0.8	CNO	5.5 ±0.9
P′C + ch	9.1 ±1.4	Fe	1.2 ±0.2
PRC	0.61 ±0.15		

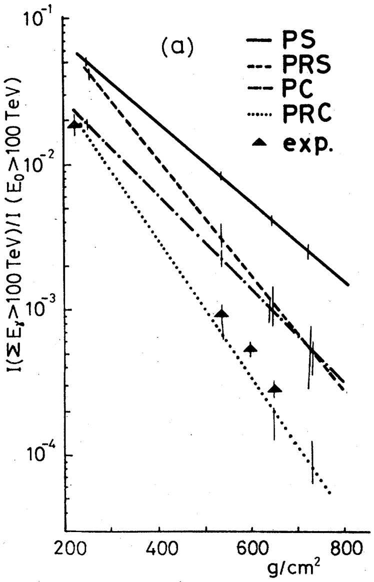

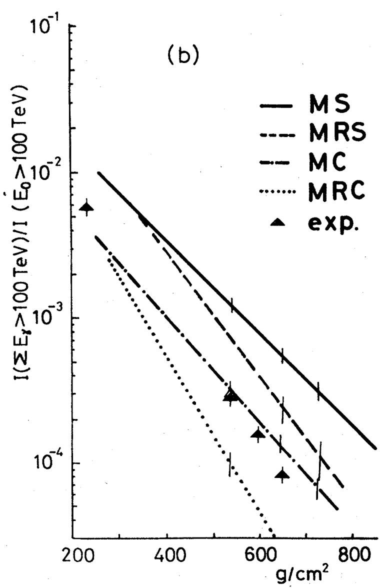

FIG. 5. (a) Altitude variation of γ-ray families of $\sum E\gamma > 100$ TeV for proton primary models. Experimental data are from Ref. 16. (b) The same as Fig. 5(a) for mixed primary models.

TABLE V. Attenuation length of γ-ray families in the atmosphere ($\sum E_\gamma > 100$ TeV).

Model	λ_{att} g/cm^2
PS	160 ±10
PRS	110 ±15
PC	140 ±10
PRC	95 ±15
MS	140 ±10
MRS	100 ±10
MC	125 ±10
MRC	85 ±20
exp	105 ±20

length. However, the assumption of the rising cross section is necessary to obtain the value of attenuation length around 100 g/cm^2.

C. Energy spectrum and multiplicity of constituent γ rays

The energy spectra of constituent γ rays are shown in Fig. 6 for some typical models only for the energy intervals of $100 < \sum E_\gamma < 200$ TeV and $1000 < \sum E_\gamma < 2000$ TeV, where the perpendicular axes represent the number of γ rays in a family. The sensitivity of the energy spectrum to the assumed models is poor in $100 < \sum E_\gamma < 200$ TeV region and every model, including others which are not shown in Fig. 6(a), is consistent with experimental data within the statistical error. But in the very-high-energy region [Fig. 6(b)], though the sensitivity is still not very large among assumed models, experimental data show exceptional behavior, which is characterized by the abundance of low-energy particles and the steepening of the spectrum in the high-energy region.

The abundance of low-energy particles can be attributed to the effect of heavy primary as shown in Fig. 6(c), where we assume a purely heavy component in primaries and the scaling law in the production spectrum. However the steepening of the spectrum indicates breakdown of scaling. Numerical details of the multiplicity are described in Table VI.

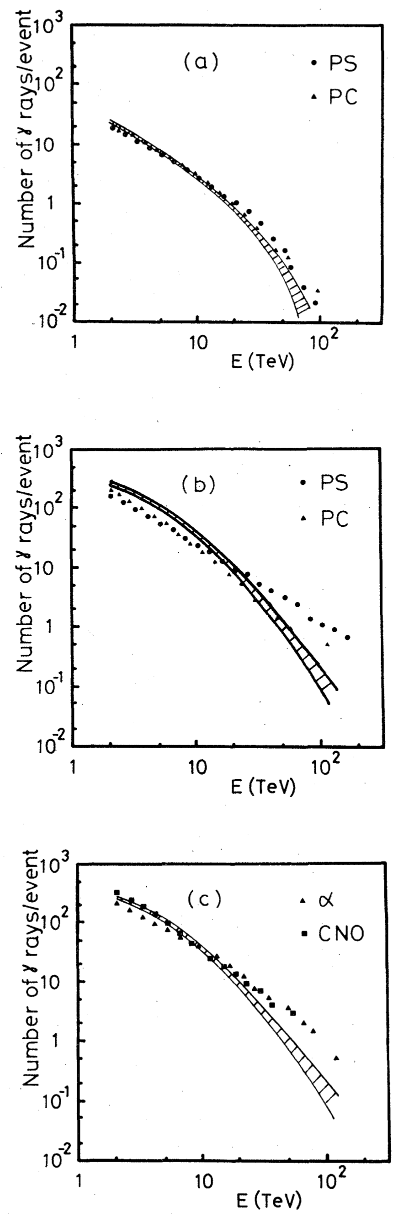

FIG. 6. Energy spectrum of constituent γ rays in a family: (a) $100 < \sum E_\gamma < 200$ TeV; (b) and (c) $1000 < \sum E_\gamma < 2000$ TeV. Hatched line represents Mt. Fuji experimental data.

D. Lateral structure of families

The average characteristics of the lateral spread of the γ-ray families are shown in Fig. 7(a) and 7(b) and Table VII, where $\langle \bar{R}_\gamma \rangle$ means that the average value of R_γ in a family is calculated for constituent γ rays and such values are averaged over many families in a given energy interval.

In Fig. 7(a) it is shown that $\langle \bar{R}_\gamma \rangle$ of the *PS* model deviates from experimental data in the high-energy region ($\sum E_\gamma > 100$ TeV) if the mean P_t is considered to be constant up to very high energy.

The effects of CKP, rising cross section, and mixed primary are in the same direction, making $\langle \bar{R}_\gamma \rangle$ larger than the *PS* model, and these assumptions with feasible combinations lead to the lateral spread consistent with experimental data up to $\sum E_\gamma \simeq 1000$ TeV without introducing the increase of mean P_t in the fragmentation region. The lateral spread of the families caused by heavy

TABLE VI. Results of simulation. Average number of γ rays and hadrons and average $\sum E_h$. The following selection criteria of families are used: $E_{\min}=2$ TeV, $n\gamma \geq 4$, $\sum E_\gamma > 30$ TeV at depth = 650 g/cm^2. Hadrons are treated as Pb jets detected in the emulsion chamber at the depths between 6 c.u. and 20 c.u. (see Sec. II J for details). The energy intervals are denoted as follows. a: $30<\sum E_\gamma<50$ TeV; b: $50<\sum E_\gamma<100$ TeV; c: $100<\sum E_\gamma<200$ TeV; d: $200<\sum E_\gamma<500$ TeV; e: $500<\sum E_\gamma<1000$.

Model		$\langle n_\gamma \rangle$	$\langle n_h \rangle$ [a]	$\langle \sum E_h \rangle$ TeV[a]
PS	a	7.8 ± 0.2	1.5 ± 0.1	9.7 ± 2.0
	b	12.1 ± 0.5	1.8 ± 0.2	15.7 ± 3.3
	c	20.7 ± 1.4	2.0 ± 0.2	14.4 ± 3.2
	d	42.5 ± 5.0	4.2 ± 0.8	55 ± 33
	e	79 ± 16	4.6 ± 1.6	41 ± 21
PRS	a	8.2 ± 0.3	1.5 ± 0.1	8.2 ± 1.2
	b	13.2 ± 0.7	1.6 ± 0.2	11.0 ± 2.6
	c	24.2 ± 1.7	2.1 ± 0.3	15 ± 4
	d	47 ± 5	2.9 ± 0.6	21 ± 8
PC	a	8.7 ± 0.3	1.6 ± 0.2	9.5 ± 2.2
	b	14.1 ± 0.8	1.9 ± 0.2	13.1 ± 3.3
	c	24 ± 2	2.9 ± 0.5	24.0 ± 7.5
	d	49 ± 7	4.2 ± 1.1	30 ± 10
PRC	a	8.6 ± 0.4	1.6 ± 0.3	8.0 ± 2.1
	b	13.8 ± 1.0	1.9 ± 0.2	12.3 ± 3.3
	c	27 ± 4	2.8 ± 0.9	25 ± 17
	d	63 ± 10	4.5 ± 1.5	36 ± 18
MS	a	8.0 ± 0.3	1.6 ± 0.1	9.4 ± 1.6
	b	12.7 ± 0.5	2.0 ± 0.2	12.7 ± 2.2
	c	23.3 ± 1.6	3.0 ± 0.4	23.4 ± 5.2
	d	45 ± 5	4.6 ± 0.9	36 ± 10
	e	100 ± 30	6.9 ± 4.3	60 ± 44
MRS	a	8.3 ± 0.3	1.6 ± 0.2	8.5 ± 1.7
	b	14.3 ± 0.8	2.0 ± 0.3	9.5 ± 1.8
	c	25 ± 2	2.5 ± 0.4	18.2 ± 6.7
	d	52 ± 10	4.2 ± 1.2	21.9 ± 7.3
	e	112 ± 34	8.3 ± 4.0	61 ± 25
MC	a	9.2 ± 0.3	1.8 ± 0.2	13.2 ± 3.2
	b	14.0 ± 0.7	2.2 ± 0.3	16.7 ± 4.1
	c	25 ± 2	3.2 ± 0.6	20.7 ± 5.1
	d	47 ± 10	3.6 ± 1.0	25 ± 10
MRC	a	8.9 ± 0.9	1.8 ± 0.4	8.2 ± 3.3
	b	15.0 ± 1.5	2.1 ± 0.4	13.5 ± 5.5
	c	24 ± 7		
α	a	8.1 ± 0.4	1.6 ± 0.2	10.0 ± 2.0
	b	13.6 ± 0.9	1.9 ± 0.3	12.3 ± 3.5
	c	24 ± 3	2.9 ± 0.6	28 ± 14
	d	50 ± 10	5.1 ± 1.3	63 ± 32
CNO	a	8.2 ± 0.4	1.8 ± 0.3	10.0 ± 3.6
	b	13.7 ± 1.2	2.6 ± 0.4	16.1 ± 3.9
	c	25.7 ± 2.8	4.1 ± 0.8	26.5 ± 8.1
	d	55 ± 9	6.7 ± 1.7	44 ± 15
	e	125 ± 27	10.9 ± 2.8	87 ± 55
FE	a	9.2 ± 0.6	2.4 ± 0.4	12.0 ± 3.1
	b	16.7 ± 1.2	3.1 ± 0.5	17.6 ± 5.4
	c	28.1 ± 3.1	5.2 ± 1.1	27.9 ± 9.2
	d	64 ± 8	9.6 ± 1.8	60 ± 16

[a] Families accompanied by no hadron are not included in statistics in these columns.

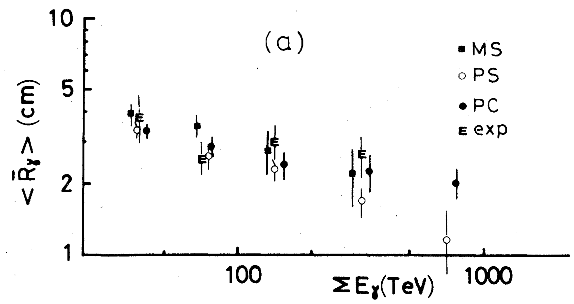

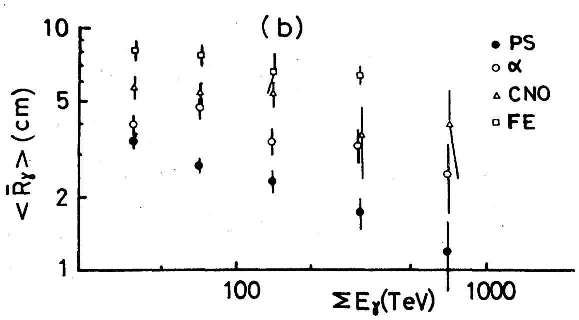

FIG. 7. Average lateral spread of γ-ray families.

primary is quite large as shown in Fig. 7(b), which strongly contradicts experimental data. Therefore the possibility of almost purely heavy primary can be rejected.

The same characteristics are seen in a quantity $\langle \overline{ER}_\gamma \rangle$ as shown in Figs. 8(a) and 8(b). These figures show that the lateral characteristics are sensitive to many model parameters and most sensitive to the kind of primary particles.

Therefore, the fluctuation of the lateral spread reflects the primary composition. The standard deviation of $\bar{R}_\gamma$ is shown in Fig. 9, where the difference between *PS* and *PC* is rather small and the *MS* model gives greater fluctuation than proton-primary models.

Experimental data lie between models of proton-primary and mixed composition. The charge-exchange process also causes greater fluctuation of lateral spread as shown in the difference between *P′S* and *P′S* + ch models. The numerical details of lateral characteristics are described in Table VII with various methods of statistical treatment.

E. Characteristics of accompanied hadrons

Although the statistics of hadrons are still poor in the experiment, a preliminary analysis of the fraction of hadron energy in a family was made using a quantity defined by

$$r_{E_{\mathrm{Pb}}} = \sum E_{\mathrm{Pb}} \Big/ \left(\sum E_\gamma + \sum E_{\mathrm{Pb}} \right) ,$$

TABLE VII. Mean values of lateral structures. R_γ in cm, E_γ in TeV. See caption of Table VI.

Model		$\langle R_\gamma \rangle$	$\langle \overline{R}_\gamma \rangle$	$\langle \log_{10} R_\gamma \rangle$	$\langle ER_\gamma \rangle$	$\langle \overline{ER}_\gamma \rangle$	$\langle \log_{10} ER_\gamma \rangle$
PS	a	3.4 ± 0.1	3.4 ± 0.2	0.27 ± 0.02	13.8 ± 0.6	14.2 ± 1.1	0.88 ± 0.02
	b	2.8 ± 0.1	2.7 ± 0.2	0.20 ± 0.02	12.0 ± 0.5	12.2 ± 0.9	0.83 ± 0.02
	c	2.5 ± 0.1	2.3 ± 0.2	0.11 ± 0.02	11.4 ± 0.6	11.5 ± 1.3	0.76 ± 0.02
	d	1.8 ± 0.1	1.7 ± 0.3	−0.06 ± 0.02	8.4 ± 0.5	8.6 ± 1.5	0.60 ± 0.02
	e	1.2 ± 0.2	1.1 ± 0.4	−0.25 ± 0.03	6.4 ± 0.8	6.2 ± 1.7	0.44 ± 0.04
PRS	a	3.5 ± 0.1	3.3 ± 0.3	0.27 ± 0.02	13.5 ± 0.6	13.6 ± 1.1	0.86 ± 0.02
	b	3.1 ± 0.1	3.1 ± 0.2	0.24 ± 0.02	14.0 ± 0.5	13.7 ± 1.2	0.85 ± 0.02
	c	2.6 ± 0.1	2.5 ± 0.3	0.14 ± 0.02	11.3 ± 0.6	11.7 ± 1.5	0.76 ± 0.02
	d	2.4 ± 0.1	2.3 ± 0.4	0.06 ± 0.02	10.6 ± 0.7	10.6 ± 1.6	0.69 ± 0.02
	e	1.8 ± 0.2	1.7 ± 1.0	−0.17 ± 0.04	8.1 ± 1.0	7.9 ± 4.8	0.45 ± 0.05
PC	a	3.5 ± 0.2	3.3 ± 0.2	0.34 ± 0.02	13.0 ± 0.6	13.1 ± 1.0	0.91 ± 0.02
	b	3.0 ± 0.2	2.9 ± 0.3	0.27 ± 0.02	11.9 ± 0.6	12.0 ± 1.2	0.86 ± 0.02
	c	2.4 ± 0.2	2.4 ± 0.3	0.14 ± 0.02	10.1 ± 0.6	10.3 ± 1.4	0.77 ± 0.02
	d	2.3 ± 0.2	2.3 ± 0.4	0.14 ± 0.03	10.0 ± 0.7	10.1 ± 1.4	0.77 ± 0.03
PRC	a	3.8 ± 0.2	3.6 ± 0.3	0.37 ± 0.03	14.3 ± 0.8	14.7 ± 1.6	0.95 ± 0.03
	b	3.4 ± 0.2	3.3 ± 0.3	0.34 ± 0.02	13.4 ± 0.8	13.6 ± 1.3	0.93 ± 0.02
	c	3.1 ± 0.3	2.8 ± 0.6	0.24 ± 0.04	12.3 ± 1.1	11.6 ± 2.2	0.84 ± 0.04
	d	2.5 ± 0.2	2.5 ± 0.4	0.19 ± 0.03	10.0 ± 0.8	10.0 ± 1.3	0.78 ± 0.03
large P_t	a	4.3 ± 0.5	4.1 ± 0.8	0.33 ± 0.06	17.3 ± 2.0	17.2 ± 3.6	0.94 ± 0.06
	b	4.1 ± 0.4	4.0 ± 0.8	0.35 ± 0.05	18.7 ± 2.1	19.6 ± 4.3	0.98 ± 0.05
	c	3.2 ± 0.5	2.9 ± 0.8	0.22 ± 0.07	17.2 ± 3.2	16.2 ± 5.0	0.93 ± 0.07
	d	3.2 ± 0.5	3.0 ± 1.8	0.21 ± 0.06	17.0 ± 3.6	17.1 ± 11	0.87 ± 0.06
$P'S$ + ch	a	4.1 ± 0.2	4.1 ± 0.4	0.33 ± 0.03	16.5 ± 0.9	16.8 ± 1.7	0.92 ± 0.03
	b	3.8 ± 0.2	3.6 ± 0.3	0.31 ± 0.02	16.4 ± 0.8	17.2 ± 1.6	0.93 ± 0.02
	c	2.8 ± 0.1	2.8 ± 0.3	0.18 ± 0.02	13.7 ± 0.8	14.5 ± 1.7	0.83 ± 0.02
	d	2.6 ± 0.1	2.6 ± 0.3	0.16 ± 0.02	12.8 ± 0.7	13.1 ± 1.4	0.80 ± 0.02
MS	a	4.0 ± 0.2	3.8 ± 0.3	0.34 ± 0.02	15.4 ± 0.7	15.4 ± 1.2	0.94 ± 0.02
	b	3.6 ± 0.1	3.4 ± 0.3	0.29 ± 0.02	15.0 ± 0.7	15.1 ± 1.5	0.90 ± 0.02
	c	3.2 ± 0.1	2.9 ± 0.3	0.23 ± 0.02	13.8 ± 0.6	13.3 ± 1.4	0.86 ± 0.02
	d	3.0 ± 0.2	2.7 ± 0.4	0.17 ± 0.02	13.6 ± 0.8	12.7 ± 2.0	0.81 ± 0.02
	e	2.3 ± 0.2	2.0 ± 1.4	−0.03 ± 0.04	10.6 ± 1.2	9.2 ± 5.8	0.62 ± 0.03
MRS	a	4.3 ± 0.2	4.1 ± 0.4	0.38 ± 0.03	16.4 ± 0.8	16.4 ± 1.6	0.96 ± 0.02
	b	4.1 ± 0.2	3.9 ± 0.4	0.34 ± 0.02	16.1 ± 0.8	15.9 ± 1.7	0.93 ± 0.02
	c	3.8 ± 0.2	3.5 ± 0.5	0.32 ± 0.02	15.9 ± 1.0	15.8 ± 2.3	0.93 ± 0.02
	d	3.4 ± 0.2	3.0 ± 0.7	0.24 ± 0.03	13.9 ± 1.0	13.2 ± 2.8	0.85 ± 0.03
	e	3.6 ± 0.3	3.2 ± 1.1	0.28 ± 0.04	14.6 ± 1.3	13.5 ± 4.2	0.87 ± 0.04
MC	a	4.0 ± 0.2	3.9 ± 0.3	0.40 ± 0.02	14.6 ± 0.7	14.8 ± 1.3	0.96 ± 0.02
	b	3.4 ± 0.2	3.2 ± 0.3	0.31 ± 0.02	13.7 ± 0.8	13.6 ± 1.3	0.91 ± 0.02
	c	3.1 ± 0.2	2.7 ± 0.5	0.23 ± 0.03	12.5 ± 0.8	11.4 ± 1.7	0.85 ± 0.02
	d	2.2 ± 0.2	2.2 ± 0.6	0.07 ± 0.03	9.1 ± 0.8	9.3 ± 2.4	0.70 ± 0.03
MRC	a	4.3 ± 0.5	4.3 ± 0.7	0.45 ± 0.04	16.3 ± 1.8	17.2 ± 2.7	1.02 ± 0.05
	b	3.7 ± 0.3	3.5 ± 0.7	0.34 ± 0.04	13.9 ± 1.3	13.5 ± 2.7	0.91 ± 0.04
	c	3.7 ± 0.5	3.3 ± 1.2	0.35 ± 0.06	14.1 ± 2.0	13.5 ± 3.5	0.96 ± 0.06
α	a	4.2 ± 0.3	4.0 ± 0.4	0.36 ± 0.04	16.5 ± 1.1	16.4 ± 1.9	0.95 ± 0.04
	b	4.7 ± 0.2	4.6 ± 0.4	0.48 ± 0.02	19.5 ± 1.1	20.2 ± 2.2	1.08 ± 0.02
	c	3.6 ± 0.2	3.4 ± 0.4	0.29 ± 0.03	15.2 ± 1.1	15.3 ± 2.3	0.91 ± 0.03
	d	3.3 ± 0.3	3.2 ± 0.5	0.29 ± 0.03	14.3 ± 1.2	14.3 ± 2.2	0.90 ± 0.03
CNO	a	5.9 ± 0.4	5.7 ± 0.5	0.59 ± 0.03	22.7 ± 1.5	23.0 ± 2.3	1.17 ± 0.03
	b	5.7 ± 0.3	5.6 ± 0.5	0.59 ± 0.02	22.7 ± 1.4	24.5 ± 3.1	1.18 ± 0.03
	c	5.3 ± 0.3	5.4 ± 0.5	0.56 ± 0.02	22.5 ± 1.3	24.0 ± 2.3	1.15 ± 0.02
	d	4.2 ± 0.3	4.0 ± 0.7	0.43 ± 0.03	17.7 ± 1.3	17.6 ± 2.6	1.03 ± 0.03
	e	3.6 ± 0.3	3.6 ± 0.4	0.30 ± 0.03	15.1 ± 1.2	15.2 ± 1.7	0.93 ± 0.03

TABLE VII. (*Continued*)

Model		$\langle R_\gamma \rangle$	$\langle \bar{R}_\gamma \rangle$	$\langle \log_{10} R_\gamma \rangle$	$\langle ER_\gamma \rangle$	$\langle \overline{ER}_\gamma \rangle$	$\langle \log_{10} ER_\gamma \rangle$
Fe	a	8.3 ± 0.4	8.1 ± 0.7	0.79 ± 0.03	31.0 ± 1.9	31.7 ± 3.2	1.35 ± 0.03
	b	7.7 ± 0.4	7.6 ± 0.6	0.75 ± 0.02	29.1 ± 1.6	29.4 ± 2.6	1.31 ± 0.03
	c	7.2 ± 0.4	7.3 ± 0.7	0.72 ± 0.03	29.4 ± 1.9	30.2 ± 3.0	1.30 ± 0.03
	d	6.1 ± 0.3	6.2 ± 0.5	0.63 ± 0.02	25.1 ± 1.6	25.3 ± 2.2	1.21 ± 0.03

where $\sum E_{\mathrm{Pb}}$ is the summation of Pb-jet energy liberated by the interaction of hadrons with the lead target of the emulsion chamber.

Fig. 10 represents the distribution of the above-defined variable for some typical models, where families accompanied by no hadron are not included. The *PS* model shows a sharp peak in the small $r_{E\mathrm{Pb}}$ region which is not seen in experimental data.

Because of the poor detection efficiency of hadrons assumed in the present calculation (hadrons are detectable only in $6 < t < 20$ c.u.), it is still difficult to describe precisely the sensitivity of characteristics of hadrons to the assumed model parameters. Figure 11 shows how the situation would be changed if we could improve the detection efficiency of hadrons using 50 c.u. as the effective thickness of the chamber instead of 20 c.u., where the average value of $\log_{10} r_{E\mathrm{Pb}}$ is plotted for given energy intervals of $\sum E_\gamma$.

The energy fraction of hadrons is much higher in the *PC* model than in the *PS* model in the $\sum E_\gamma > 100$ TeV region; the *MS* model lies between them.

F. Character of rejuvenated families

1. f' spectrum

The sensitivities of the f' spectrum to the production model and the primary chemical composition are tested and they are shown in Fig. 12 for different energy intervals with $f'_m = 0.04$. Figure

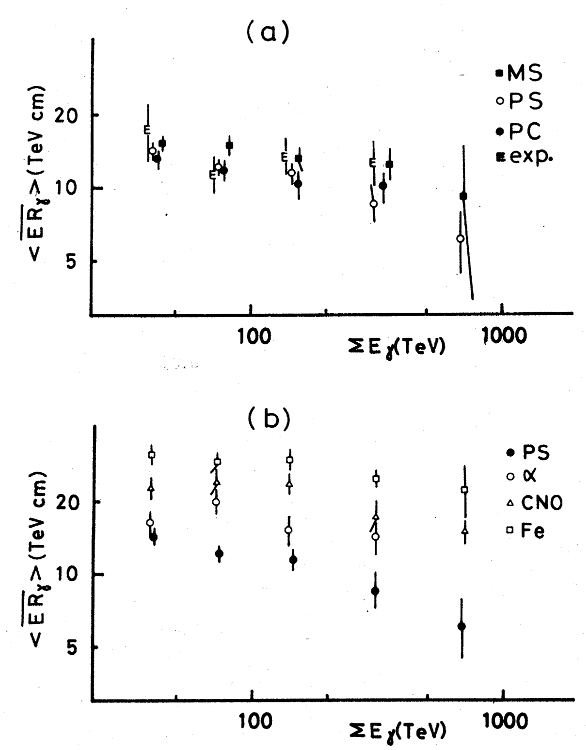

FIG. 8. Average *ER* of γ-ray families.

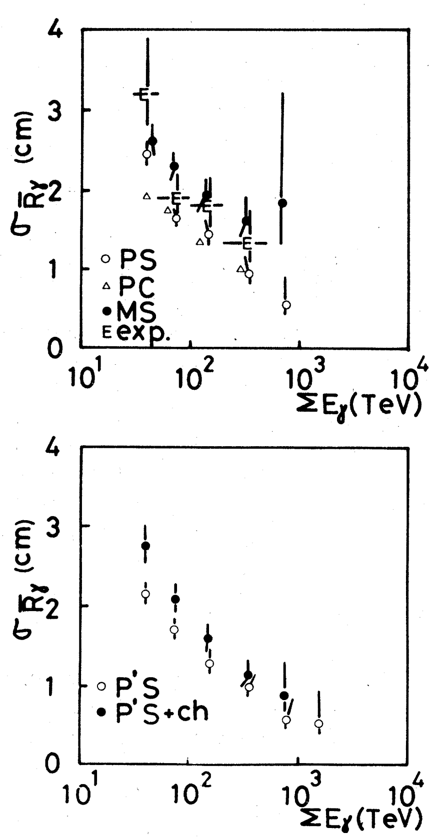

FIG. 9. Fluctuation of lateral spread in γ-ray families.

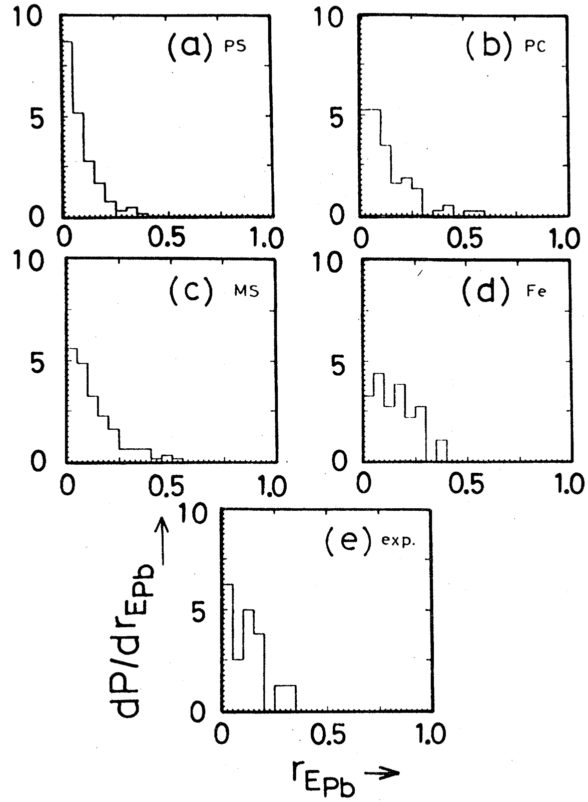

FIG. 10. Distribution of the fraction of hadron energy to the total energy of a family ($100<\sum E\gamma<200$ TeV).

12 shows that the invariance of f' spectrum still holds in the CKP model within the statistical error. In Figs. 12(c)–12(e) are shown the behavior of the f' spectrum under the assumption of heavy primaries, where the invariance does not hold. The degree of the break of invariance becomes larger when the mass number of primary increases. Experimental data [Fig. 12(f)] are consistent with the *PS* or *PC* model in low energy

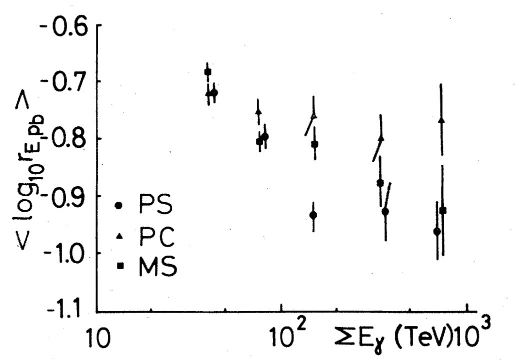

FIG. 11. Average value of $\log_{10} r_{E_{\mathrm{Pb}}}$ in given energy intervals. Effective thickness of the chamber is assumed as 50 c.u.

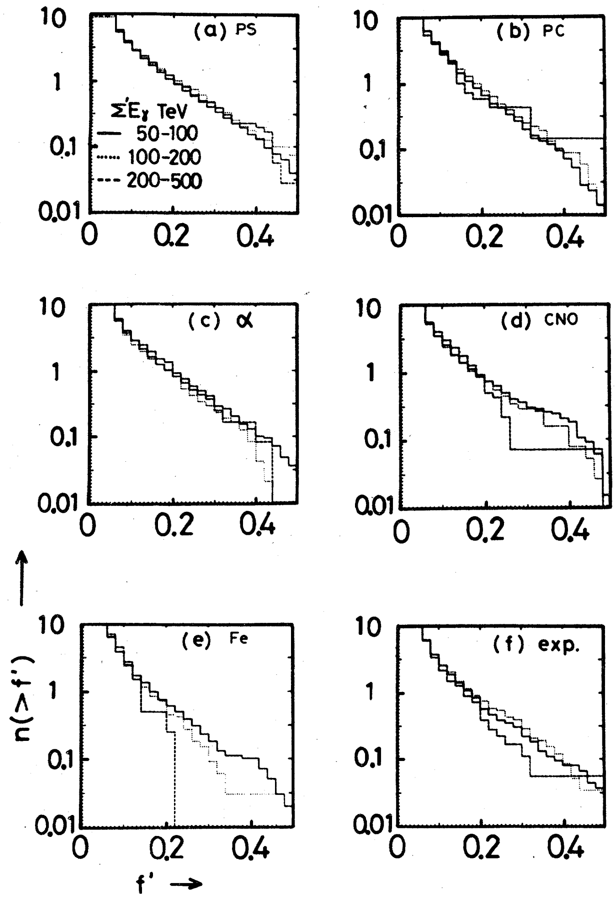

FIG. 12. f' spectra of γ-ray families. Energy interval and notations are shown in Fig. 12(a). $f'_m=0.04$.

and it shows slight deviation from them in the highest-energy interval ($200<\sum' E_\gamma<500$ TeV); however the statistics and accuracy of the energy determination in this region make the discussion inconclusive.

The average multiplicity of a rejuvenated family is shown in Table VIII, where the experimental data are consistent with models which assume the CKP model and/or dominance of heavy primary. But it is worth noticing that no model shows the apparent increase of $\langle n'\rangle$ with energy.

2. *Azimuthal asymmetry*

The azimuthal asymmetry of the family can be expressed by the formula[6(a)]

$$b=\sum E_i Y_i^2 \Big/ \sum E_i X_i^2 ,$$

where the X axis is taken to minimize $\sum E_i Y_i^2$. The average values of b for rejuvenated families (b') with $f'_m=0.04$ are plotted for various models in Fig. 13 as a function of $\langle n'\rangle$ in the total energy

TABLE VIII. Average multiplicity of rejuvenated families with $f'_m = 0.04$. The number of events is given in parentheses.

Model \ $\sum E_\gamma$ (TeV)	$\langle n' \rangle$ 50–100	100–200	200–500
PS	9.8 ±0.3 (507)	9.2 ±0.6 (121)	9.5 ±1.1 (36)
PRS	10.2 ±0.3 (397)	10.2 ±0.7 (102)	11.1 ±1.7 (20)
PC	11.0 ±0.4 (214)	10.7 ±0.6 (69)	10.0 ±3.0 (7)
PRC	10.8 ±0.6 (140)	11.4 ±1.2 (32)	
MS	10.0 ±0.3 (405)	10.1 ±0.6 (120)	9.8 ±1.2 (31)
MRS	11.1 ±0.4 (261)	10.3 ±1.0 (64)	9.4 ±2.1 (11)
MC	11.0 ±0.4 (214)	11.3 ±0.8 (49)	
α	10.3 ±0.5 (166)	10.7 ±1.0 (47)	10.8 ±2.1 (12)
CNO	10.7 ±0.6 (132)	10.8 ±1.3 (38)	10.3 ±2.3 (14)
Fe	11.8 ±0.6 (99)	12.2 ±1.0 (33)	
exp	10.8 ±0.6 (136)	10.9 ±0.9 (58)	12.7 ±2.1 (18)

region. Though the statistics are still poor, some of the models survived by the comparison of other characteristics are out of the statistical error of the experimental data, for example the *MC* model.

Generally, symmetry is too high in the CKP model; on the other hand, the value of $\langle n' \rangle$ is too

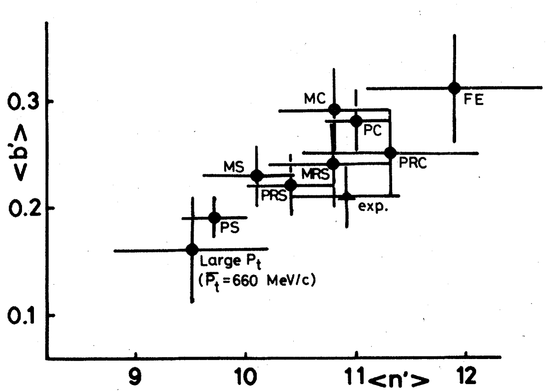

FIG. 13. Azimuthal-asymmetry coefficient as a function of $\langle n' \rangle$. Results are from whole energy region $f'_m = 0.04$.

TABLE IX. Multiplicity and azimuthal asymmetry coefficient for rejuvenated families in total energy interval.

Model	Multiplicity	Asymmetry coefficient
PS	9.7 ± 0.3	0.19 ± 0.02
PRS	10.4 ± 0.4	0.22 ± 0.03
PC	11.0 ± 0.3	0.28 ± 0.03
PRC	11.3 ± 0.8	0.25 ± 0.04
MS	10.1 ± 0.5	0.23 ± 0.03
MRS	10.8 ± 0.6	0.24 ± 0.04
MC	10.8 ± 0.5	0.24 ± 0.04
MRC	11.9 ± 1.7	0.35 ± 0.12
α	10.4 ± 0.4	0.23 ± 0.03
CNO	10.6 ± 0.7	0.25 ± 0.04
Fe	11.9 ± 0.8	0.31 ± 0.05
PS and P_t = 660 MeV/c	9.5 ± 0.7	0.16 ± 0.05
exp	10.9 ± 0.5	0.21 ± 0.03

small in the scaling model. Here, the effect of large P_t was also tested with a mean P_t of 660 MeV/c (other parameters are standard). It is seen that large P_t can reduce the value of b'; it is understood as the effect of the limited size of the observation area (see Sec. II J). The numerical values of $\langle b' \rangle$ are listed in Table IX together with $\langle n' \rangle$ of the total energy interval.

The small values of $\langle b' \rangle$ in scaling models are connected with the sharp peak in the small-b' region in its distribution as shown in Fig. 14. The CKP model [Fig. 14(b)] does not show such a sharp peak, and heavy primary decreases the peak rapidly with increasing mass number as shown in Fig. 14(d). The distribution form of the experimental data is an interesting one as shown in Fig. 14(g); it has a sharp peak in the small-b' region but the behavior in other regions is not similar to any model calculations.

If we introduce any asymmetric characteristic in the production mechanism, say jet production, the above-mentioned discussion will be changed and the CKP model and/or dominance of heavy primaries would be able to give $\langle b' \rangle$ values which are consistent with the experimental data.

IV. INFORMATIONS ON ORIGIN OF FAMILIES

A. Primary particles of observed families

Further investigation was made of the origin of the families. In the *MS* model, the type of the primary particle was investigated for observed families of given energy intervals. The contribution of each chemical component is shown in Table X. In spite of the low abundance of protons in the mixed primary model, about 75% of the families

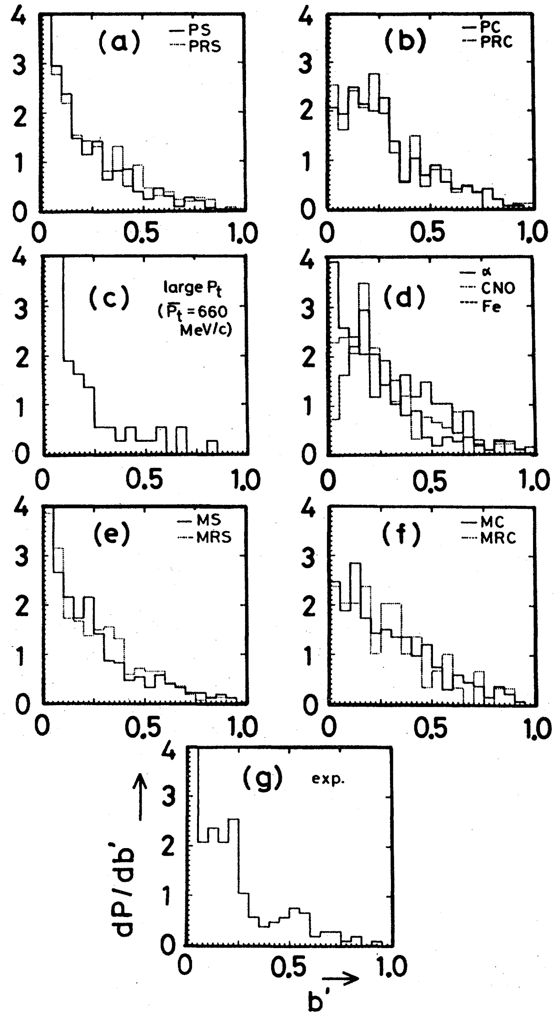

FIG. 14. Distribution of azimuthal-asymmetry coefficient.

are generated by protons.

The distributions of the primary energies which created the γ-ray families of $\sum E_\gamma > 100$ TeV are shown in Fig. 15 for *PS*, *PC*, and α models, and

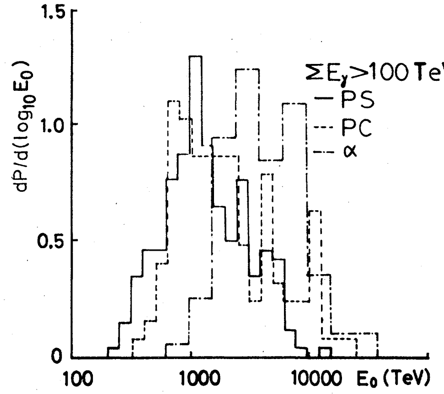

FIG. 15. Distribution of primary energy contributing to families of $\sum E\gamma > 100$ TeV.

their average values are shown in Table XI with some other models. These values are apparently dependent on the mass number of primaries; therefore if there were information on primary energy of the observed families we could also investigate the primary composition. This suggests the desirability of cooperation of an air-shower array with an emulsion-chamber experiment.

B. Purity and main interaction height

Each particle in a family was traced back to its origin and classified to the individual interaction above the observation level. Finally, the most responsible interaction for detected family energy was found and called the main interaction.

Purity is defined as the fraction of the energy coming from the main interaction to the total observed energy. Figure 16(a) shows the mean value of purity of the γ-ray family for some typical models at 650 g/cm^2 as a function of $\sum E_\gamma$. The purity decreases with increasing energy; in other words, the contamination of old generations in nuclear cascades becomes higher in the high-energy region. Therefore the electromagnetic cascade becomes a dominant process which masks any non-

TABLE X. Parent particle of observed families in the *MS* model (385 events).

$\sum E_\gamma$ (TeV)	p	α	L	M	LH	MH	VH
30–50	132	13	0	13	4	1	5
50–100	96	7	0	14	7	1	3
100–200	39	5	0	5	4	0	2
200–500	23	4	0	1	1	0	0
500–1000	3				1		
1000–2000	1						
Total	294	29	0	33	17	2	10
Percent	76.4	7.5	0	8.6	4.4	0.5	2.6

TABLE XI. Average primary energy contributing to families of $\sum E_\gamma > 100$ TeV.

Model	$\langle E_0 \rangle$ (TeV)
PS	1530 ± 180
PRS	2550 ± 520
PC	2210 ± 430
PRC	5200 ± 3300
α	4500 ± 780
CNO	7800 ± 1700
Fe	15400 ± 2900

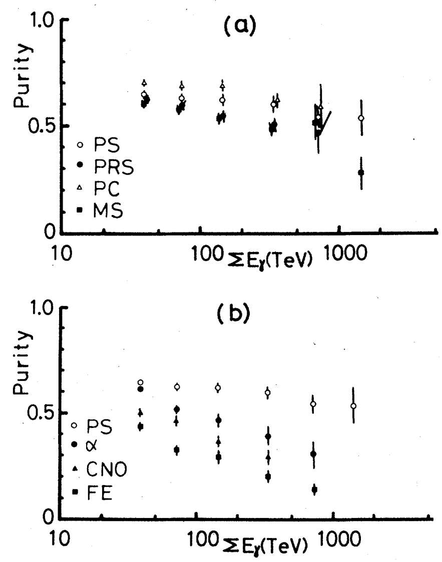

FIG. 16. Average purity as a function of $\sum E\gamma$ at Mt. Fuji level.

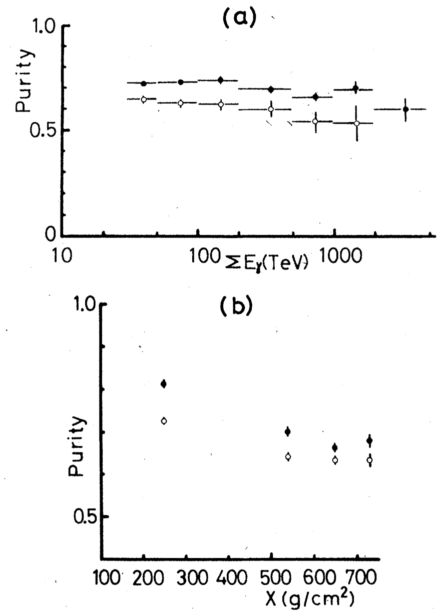

FIG. 17. (a) Average purity for *PS* model as a function of $\sum E\gamma$, closed circle for 250 g/cm^2, open circle for 650 g/cm^2. (b) Altitude variation of average purity for *PS* model, closed circle for rejuvenated families, open circle for nonrejuvenated families in total energy interval.

scaling characteristic of the elementary interaction. In Fig. 16(a), the *PC* model gives the highest purity among calculated results; the assumptions of rising cross section and dominance of heavy primary decrease the purity. Figure 16(b) shows primary mass-number dependence of purity (at 650 g/cm^2).

It is expected that the purity is much higher at the observation level with small atmospheric depth. Figure 17(a) shows the comparison of the average purity at 250 g/cm^2 with that of 650 g/cm^2 for the standard model (*PS*). The difference is seen but it is not very large. Figure 17(b) also shows the altitude variation of the purity by the *PS* model, where the average value in whole energy intervals is used; it becomes almost constant at the mountain altitude (equilibrium state). The effect of rejuvenation is also shown by closed circles in the same figure, describing the degree of improvement of the purity by the rejuvenation procedure.

The main interaction height is distributed over a wide range of atmospheric depths as shown in Fig. 18(a) for the *PS* model in the whole energy interval (at 650 g/cm^2) with a mean value of 140 ± 3 g/cm^2 (1.9 km), where the horizontal axis represents the main interaction height from the observation level in the unit of g/cm^2. About one-half of the observed families have the main interaction height less than 2 km, but another half ranges up to 10 km. The same is shown in Fig. 18(b) for the *PC* model whose mean value is 125 ± 4 g/cm^2 (1.6 km). The mean values of the main interaction height at various altitudes are plotted

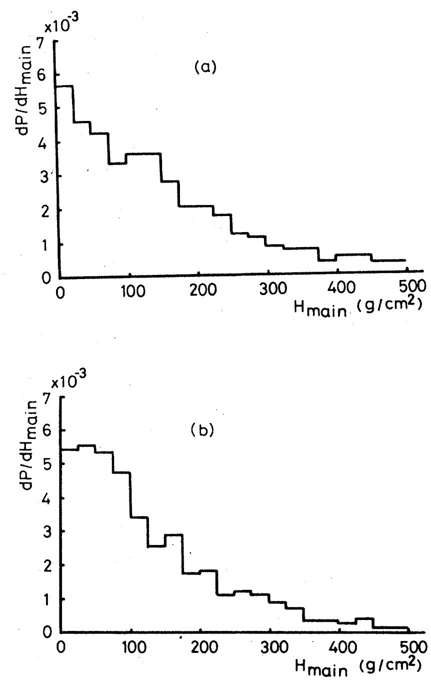

FIG. 18. Main-interaction-height distribution at Mt. Fuji level; (a) *PS* model, (b) *PC* model in total energy interval.

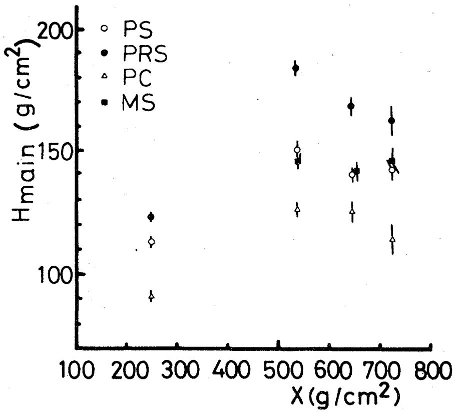

FIG. 19. Altitude variation of main interaction height (averaged over total energy interval).

in Fig. 19 for some models.

Figures 18 and 19 tell us that the interaction height of the family is also dependent on the assumed model parameters and its fluctuation is fairly large.

V. COMPARISON WITH OTHER CALCULATIONS

Though the details of calculation are different in other existing works, the comparison of basic results is made with the present work. The frequency of the generation of γ-ray families is compared and shown in Table XII in terms of the fraction $I(\sum E_\gamma > 100\ \text{TeV})/I(E_0 > 100\ \text{TeV})$, where the *PS* model by Wrotniak[6(a)] assumes slightly different primary intensity from ours and observation is made at 600 g/cm^2 and the *MS* model by Kasahara, Torii, and Yuda[5] assumes different chemical composition. Taking into account these differences, the calculations are all in good agreement.

Another basic quantity is the multiplicity of the γ rays in a given energy interval, which is very weakly dependent on model parameters. They are shown in Table XIII, where we can also see good agreement.

Lateral characteristics are so deeply related to the details of the calculation as described in Sec. III D that it should be compared with a result from almost exactly the same assumptions, which is not available at present. But their sensitivity to the assumed model parameters is quite consistent among all works cited above.

TABLE XII. Comparison of the efficiency of family generation with other works. The efficiency is expressed by $I(\sum_\gamma > 100\ \text{TeV})/I(E_0 > 100\ \text{TeV})$.

Model	Present work	Kasahara *et al.*[5]	Wrotniak[6(a)]
PS	3.95×10^{-3}		3.32×10^{-3}
P'S	5.42×10^{-3}	$5\ \ \times10^{-3}$	
P'C	1.50×10^{-3}	1.2×10^{-3}	
MS	6.77×10^{-4}	$9\ \ \times10^{-4}$	
Fe	$1.0\ \ \times10^{-4}$	1.1×10^{-4}	

VI. CONCLUSION

It is already clear that the standard model (*PS*) cannot reproduce the experimental data because of the contradicted behaviors in the $\sum E_\gamma$ intensity, the lateral spread, and the attenuation length of energy flow in the atmosphere compared with the experimental data.

To explain these contradictions, several possibilities such as rising cross section, dominance of heavy primary, violation of scaling law, large P_t, and charge-exchange probability are examined related to various aspects of the characteristics of γ-ray families.

Some of these additional assumptions bring similar effects into calculated results; for example, most of the resultant effects of scaling violation are similar to those of heavy primary as is seen in $\sum E_\gamma$ intensity, f' spectrum, and lateral structures.

The same holds for other model parameters. It is possible to reproduce experimental data by the *MRS* model, where intense dominance of heavy primaries in the high-energy region and the very strong increase of interaction cross section ($\sigma \propto E_0^{0.06}$) are assumed on the basis of the validity of the scaling law. On the other hand, *PRC* and *MC* models also show a high possibility of explaining most of the characteristics of families if we additionally include an assumption of large

TABLE XIII. Comparison of the multiplicity of constituent γ rays in a family. Rejuvenated multiplicities (n') are given in parentheses.

$\sum E_\gamma$ (TeV)	Present work	Wrotniak[6a]	Dunaevskii *et al.*[6(b)]
30–50	7.8 ± 0.2	7.6 ± 0.2	7.4 ± 0.1
50–100	12.1 ± 0.5 (9.8 ± 0.3)	12.3 ± 0.3 (9.6 ± 0.2)	12.1 ± 0.3 (9.4 ± 0.3)
100–200	20.7 ± 1.4 (9.2 ± 0.6)	22.6 ± 0.8 (9.9 ± 0.3)	20.6 ± 1.0 (9.4 ± 0.3)
200–500	$42.5 \pm 5\ 0$ (9.5 ± 1.1)	39.3 ± 2.1 (9.2 ± 0.5)	$40\ \ \pm 3$ (9.4 ± 0.4)

P_t or an azimuthally asymmetric mechanism in the elementary process. But there are some results which are free from such an ambiguity as described above.

The magnitude of lateral fluctuation (Fig. 9) shows that the mixed-composition model used in the present calculation is the upper boundary of the abundance of heavy nuclei among primaries.

The attenuation length of $\sum E_\gamma$ intensity in the atmosphere also shows clearly the effect of rising cross section; Fig. 5 implies that there should be an increase of the interaction cross section with increasing E_0. Though the formula $\sigma \propto E_0{}^\delta$ ($\delta = 0.06$) is used in the present calculation, a mild extrapolation of the accelerator data may be expressed by a smaller value of δ, say $0.02 \sim 0.03$. If we come to the assumptions of such a smaller value of δ and less abundance of heavy primaries than the previously discussed one, then the violation of scaling in the fragmentation region becomes an important factor in reproducing experimental data. Also the existence of azimuthally asymmetric phenomena is strongly suggested.

ACKNOWLEDGMENTS

The author is grateful to the members of the Mt. Fuji group for allowing the use of experimental data. He owes greatly to Dr. Kasahara, Dr. Torii, and Professor Yuda of the Institute of Cosmic Ray, University of Tokyo, for continuous encouraging and fruitful discussions benefiting this work. The author thanks Mr. E. Nagata of Yokohama National University for help in the calculations. This work was supported by Contract No. FACOM M-180 AD II of the Institute of Nuclear Study of the University of Tokyo and Contract No. FACOM M-150F of Yokohama National University.

APPENDIX: SAMPLING METHOD IN PARTICLE PRODUCTION

In the procedure of sampling particle production, it is necessary to take into account energy conservation. Suppose that we assume an inclusive energy spectrum of particle production and multiplicity distribution; then we repeat the sampling until the sum of the sampled energies conserves energy to within some predetermined accuracy.

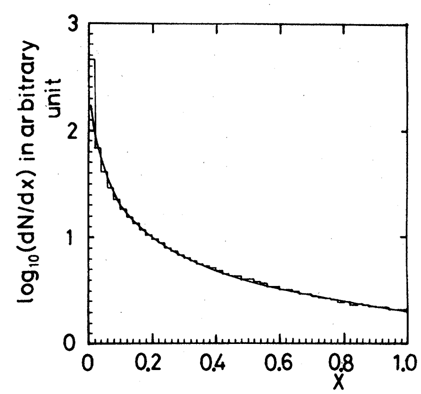

FIG. 20. Sampled distribution of x from uniform sampling function with a condition (A1). Solid curve represents $1/x$.

Then, there must be a distortion in the sampled energy spectrum because some cases of sampling are rejected by wrong conservation of energy. Such a problem always exists when we use an inclusive spectrum (not exclusive).

In the present paper, the sampling was made as follows:

A distribution function $\psi_s(x)dx$ is assumed as a sampling function and the kth value of x is sampled with a condition expressed as

$$x_k < 1 - \sum_{i=1}^{k-1} x_i \,. \tag{A1}$$

Such a condition of course distorts the assumed distribution $\psi_s(x)$, but we can know how the spectrum is distorted. For example, it was tested that we get the sampled distribution close to $\psi(x)dx \simeq dx/x$ when we assume uniform distribution $\psi_s(x)dx = dx$ as shown in Fig. 20.

Using an analogy to this case, sampling was made assuming the sampling function $\psi_s(x)dx = x\psi(x)dx$, where $\psi(x)dx$ is the distribution function which we want to obtain as a result of the sampling. Sampling was repeated until the right-hand side of (A1) becomes less than $x_{\min}(=E_{\min}/E_0)$. Therefore the multiplicity is defined only for particles above minimum energy. The results of sampling are in good agreement with physically assumed distribution in the present paper, as shown in Figs. 2 and 3.

[1] K. Niu, Nuovo Cimento 10, 944 (1958); P. Ciok, T. Coghen, J. Gierula, R. Holynski, A. Jurak, M. Miesowiez, T. Saniewska, O. Stanisz, and J. Pernegr, Nuovo Cimento 8, 166 (1958); 10, 741 (1958); G. Cocconi, Phys. Rev. 111, 1699 (1958).

[2] R. P. Feynman, Phys. Rev. Lett. 23, 1415 (1969).

[3] J. Benecke, T. T. Chou, C. N. Yang, and E. Yen, Phys. Rev. 188, 2159 (1969).

[4] Mt. Fuji Emulsion Chamber Experiment, in *Sixteenth International Cosmic Ray Conference, Kyoto, 1979,*

Conference Papers (Institute of Cosmic Ray Research, University of Tokyo, 1979), Vol. 7, pp. 68, 284, 294; Vol. 13, pp. 87, 92, 98.

[5]Preliminary results are given in K. Kasahara, S. Torii, and T. Yuda, in *Sixteenth International Cosmic Ray Conference, Kyoto, 1979, Conference Papers* (Ref. 4), Vol. 13, pp. 70, 76.

[6](a) A. Kryś, A. Tomaszewski, and J. A. Wrotniak, Zesz. Nauk. Uniw. Lodz. Ser. 2 60, 157 (1977); J. A. Wrotniak, *ibid.* 60, 165 (1977); 60, 175 (1977); in *Pamir Collaboration Workshop, 1980,* edited by J. A. Wrotniak (University of Lodz, Poland, 1980), pp. 55, 56; (b) A. M. Dunaevskii, Ju. A. Emelyanov, B. F. Shorin, M. A. Tashimov, and A. V. Urysson, Report No. FIAN N206, 1978, P. N. Lebedev Physical Institute, Moscow (unpublished). Model M4 (according to author's notation) is used, where the details of assumptions are a little different from the present work.

[7]E. Juliusson, in *Proceedings of the Fourteenth International Conference on Cosmic Rays, Munich, 1975,* edited by Klauss Pinkau (Max-Planck-Institut, München, 1975), p. 2689.

[8]G. Cocconi, L. G. Koester, and D. H. Perkins, Lawrence Radiation Laboratory, High Energy Physics Study Seminars, Report No. 28.2 (UCID-1444, 1, 1961) (unpublished).

[9]Collaboration of the Experiment "Pamir", in *Proceedings of the Fourteenth International Conference on Cosmic Rays, Munich, 1975* (Ref. 7), p. 2370.

[10]S. A. Stephens, in *Sixteenth International Cosmic Ray Conference, Kyoto, 1979, Conference Papers* (Ref. 4), Vol. 10, p. 90.

[11]C. Bradt and B. Peters, Phys. Rev. 77, 54 (1950). Parameters are derived by fitting the following data: K. R. V. Nair, C. J. Waddington, and P. S. Freier, in *Sixteenth International Cosmic Ray Conference, Kyoto, 1979,* Ref. 4, Vol. 6, p. 216; S. P. Denisov, S. V. Donskov, Yu. P. Gorin, R. N. Krasnokotsky, A. I. Petrukgin, Yu. D. Prokoshkin, and D. A. Stoyanova, Nucl. Phys. B61, 62 (1973).

[12]A. Bialas, M. Bleszynski, and W. Czys, Nucl. Phys. B111, 461 (1976).

[13]P. S. Freier and C. J. Waddington, Astrophys. Space Sci. 38, 419 (1975).

[14]B. Rossi and K. Greisen, Rev. Mod. Phys. 13, 240 (1941).

[15]B. Rossi, *High Energy Particles* (Prentice-Hall, New York, 1952).

[16]Experimental data at 225 g/cm^2, Extrapolation of the data by E. A. Kanevska, Yu. A. Smorodin, in *Proceedings of the Fifteenth International Conference on Cosmic Rays, Plovdiv, 1977,* edited by B. Betev (Bulgarian Academy of Sciences, Sofia, 1977), Vol. 7, p. 436; at 540 g/cm^2, Japan-Brazil Collaboration, Report No. ICR-Report-81-80-3, Institute for Cosmic Ray Research, University of Tokyo, 1980 (unpublished); at 600 g/cm^2, Ref. 9.